Nano Research 2015, 8(10): 3332–3341
DOI 10.1007/s12274-015-0833-8
Research Article
ISSN 1998-0124
CN 11-5974/O4

Wafer-scale arrayed p-n junctions based on few-layer epitaxial GaTe

Xiang Yuan[1,§], Lei Tang[1,§], Peng Wang[2], Zhigang Chen[3], Yichao Zou[3], Xiaofeng Su[4], Cheng Zhang[1], Yanwen Liu[1], Weiyi Wang[1], Cong Liu[2], Fansheng Chen[4], Jin Zou[3,5], Peng Zhou[6], Weida Hu[2] (✉), and Faxian Xiu[1] (✉)

[1] *State Key Laboratory of Surface Physics and Department of Physics, and Collaborative Innovation Center of Advanced Microstructures, Fudan University, Shanghai 200433, China*
[2] *National Laboratory for Infrared Physics, Shanghai Institute of Technical Physics, Chinese Academy of Sciences, Shanghai 200083, China*
[3] *Materials Engineering, The University of Queensland, Brisbane QLD 4072, Australia*
[4] *Satellite Remote Sensing Laboratory, Shanghai Institute of Technical Physics, Chinese Academy of Sciences, Shanghai 200083, China*
[5] *Centre for Microscopy and Microanalysis, The University of Queensland, Brisbane QLD 4072, Australia*
[6] *State Key Laboratory of ASIC and System, Department of Microelectronics, Fudan University, Shanghai 200433, China*
[§] *These authors contributed equally to this work.*

Received: 15 April 2015
Revised: 6 June 2015
Accepted: 8 June 2015

KEYWORDS
GaTe,
wafer-scale
two-dimensional materials,
p-n junction,
imaging,
photodiode,
photosensor

ABSTRACT

Two-dimensional (2D) materials have attracted substantial attention in electronic and optoelectronic applications with the superior advantages of being flexible, transparent, and highly tunable. Gapless graphene exhibits ultra-broadband and fast photoresponse while the 2D semiconducting MoS_2 and GaTe exhibit high sensitivity and tunable responsivity to visible light. However, the device yield and repeatability call for further improvement to achieve large-scale uniformity. Here, we report a layer-by-layer growth of wafer-scale GaTe with a high hole mobility of 28.4 $cm^2/(V·s)$ by molecular beam epitaxy. The arrayed p-n junctions were developed by growing few-layer GaTe directly on three-inch Si wafers. The resultant diodes reveal good rectifying characteristics and a high photovoltaic external quantum efficiency up to 62% at 4.8 μW under zero bias. The photocurrent reaches saturation fast enough to capture a time constant of 22 μs and shows no sign of device degradation after 1.37 million cycles of operation. Most strikingly, such high performance has been achieved across the entire wafer, making the volume production of devices accessible. Finally, several photoimages were acquired by the GaTe/Si photodiodes with reasonable contrast and spatial resolution, demonstrating the potential of integrating the 2D materials with silicon technology for novel optoelectronic devices.

Address correspondence to Faxian Xiu, faxian@fudan.edu.cn; Weida Hu, wdhu@mail.sitp.ac.cn

1 Introduction

Graphene has recently attracted exceptional attention because of its high carrier mobility [1], broadband photon absorption [2], low dissipation rate [3], and compatibility with silicon processes [4], thus showing a great potential for electronic and optoelectronic applications, such as ultrafast [5, 6] and broadband [7] photodetectors [8]. However, the gapless band structure of graphene significantly hinders the effective modulation of channel resistance [9], making high-performance logical devices inaccessible. On the other hand, two-dimensional (2D) semiconductors, such as MoS_2 and GaTe, exhibit intriguing prospects in field-effect transistors [10–12] and p-n junctions [13–14], largely attributed to their direct bandgap [15], high absorption coefficient, and electrical tunability [16, 17]. Indeed, p-n junctions made from electrostatic doping [18] and layer stacking [19–26] have recently been realized for applications in solar cells [27], photodetectors [28], light-emitting diodes [18, 29], and photocatalysts [30]. In particular, remarkable progress has been made for MoS_2 photodetectors: MoS_2 photoconductors exhibit a high responsivity of 880 A/W [31]; chemically doped MoS_2 p-n junctions exhibit a good detectivity of 1010 at 1.5 V [32]; combined with graphene [33] and WSe_2 [34], MoS_2 vertical heterojunctions exhibit external quantum efficiencies (EQEs) of 55% and 34%, respectively. In parallel with these efforts, emerging 2D GaTe photoconductors with good photosensitivity were reported recently [35], suggesting another appealing use of 2D materials for optoelectronic applications. However, to date, GaTe photodetectors involving hetero p-n junctions for faster photoresponse in the microsecond range have not yet been demonstrated.

To date, most 2D semiconductors are prepared by mechanical exfoliation and chemical vapor deposition (CVD). Because of their small lateral scale, they require a dedicated fabrication process, thus presenting a challenge for the mass production of integrated devices. Molecular beam epitaxy (MBE), however, can be potentially employed for the growth of 2D hetero-structures with the capability of selecting the desired functional layers and developing large-scale, uniform, and reliable epitaxial films.

Here, we report a layer-by-layer epitaxial growth of wafer-scale 2D GaTe thin films using MBE and the fabrication of arrayed photodiodes devices. The *in situ* reflection high-energy electron diffraction (RHEED) provides precise control of the film thickness. The as-grown few-layer GaTe possesses a p-type conductivity with a carrier concentration of 2.5×10^{18} cm^{-3} and a high mobility of 28.4 $cm^2/(V \cdot s)$ at room temperature. The vertical p-n junctions formed by directly depositing GaTe on the Si wafers result in broadband photodiodes that respond to the entire visible spectrum, thus enabling the image acquisition of real objects. At a wavelength of 632.8 nm, the diodes exhibit a clear photovoltaic effect with an EQE up to 62% under zero bias. Notably, for photodiodes, the EQE is typically less than 100%. The response time of 22 μs to the laser illumination is also fast compared with other 2D semiconductor devices. Combined with the endurable 1.37 million operations, our heterojunction photodiodes exhibit fast, stable, and robust photoresponse.

2 Results and discussion

To characterize the electrical and optical properties of GaTe, mica was selected as a suitable substrate because of its electrical insulation and high transparency. The atomically flat surface also makes it an ideal substrate for the van der Waals epitaxial growth [36]. In this study, 2D GaTe thin films with several layers in thickness were directly grown on the freshly cleaved mica substrates layer-by-layer, monitored by *in situ* RHEED. Here, the term "layer" refers to one unit cell or a so-called quadruple layer consisting of Te–Ga–Ga–Te [37]. Figure 1(a) presents a plot of the *in situ* RHEED oscillations acquired from GaTe, indicative of inheriting the 2D growth mode in the GaTe system. The growth time for each quadruple layer was 2.33 min, thus enabling fine control of the thickness. The inset of Fig. 1(a) reveals a sharp and streaky RHEED pattern of an 8 nm GaTe thin film, indicative of a highly crystalline and atomically flat surface. Consistent with the RHEED observations, atomic force microscopy (AFM) reveals further evidence of the terrace structures on the growth front with a step of 0.8 nm, corresponding to the single-layer thickness of GaTe [37] (Fig. 1(b)). The root mean square

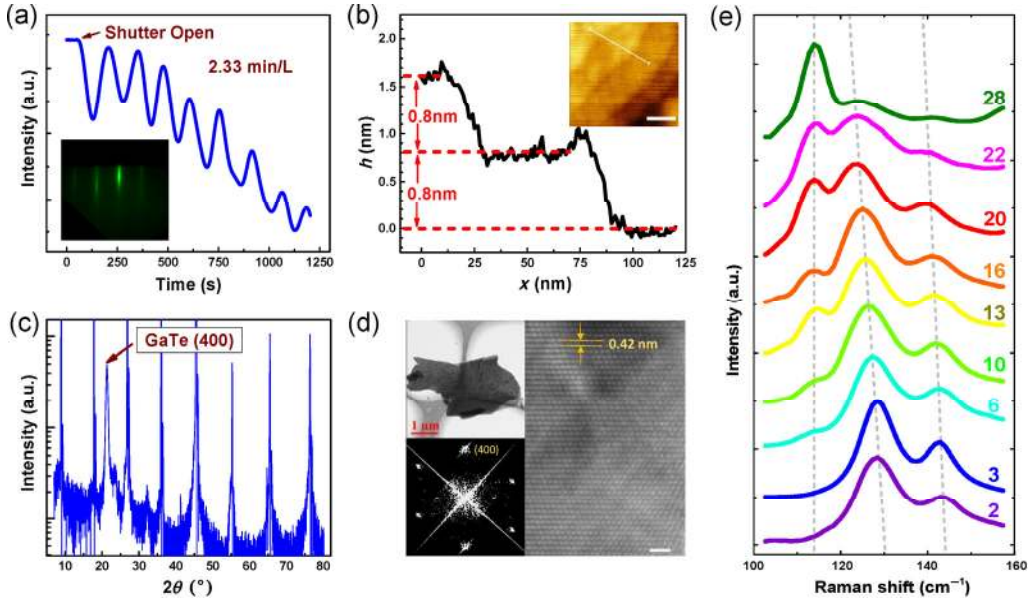

Figure 1 Growth, structural properties, and thickness-dependent Raman spectra of the few-layer GaTe thin films. (a) RHEED intensity oscillations. The persistent oscillations serve as strong evidence of layer-by-layer growth. The growth rate was determined to be 2.33 min/layer. The inset presents a sharp and streaky RHEED pattern for an 8-nm-thick GaTe film, indicative of high crystalline quality. (b) The height profile across different terraces on the sample surface. The step of 0.8 nm corresponds to the thickness of one quadruple layer in GaTe. The inset presents an AFM image showing flat terraces with an RMS less than 1.5 Å. The scale bar is 50 nm. (c) A typical XRD pattern of GaTe. The marked peak is identified as the GaTe (400) plane; the other peaks originate from the mica substrate. (d) An HRTEM image of a GaTe thin flake on a holey copper grid revealing superior crystalline quality (top view of GaTe (400), and the scale bar presents 1 μm). The inset presents a low-magnification TEM image and fast Fourier-transform (FFT) image. (e) Raman spectra for GaTe with different thickness. The number of layers is labeled. As the film thickness increases, the peak at 114 cm^{-1} emerges, and the distance between the left two peaks decreases.

(RMS) for each terrace has a small value of 1.5 Å, which reaches the ultimate resolution of our AFM.

To study the structural properties of the GaTe thin films, X-ray diffraction (XRD) and high-resolution transmission electron microscopy (HRTEM) were performed at room temperature. Figure 1(c) presents an XRD spectrum, in which the periodic diffraction peaks originate from the mica substrate, and the marked diffraction peak can be indexed as the (400) atomic plane of a monoclinic layered structure with *C*2/*m* space-group symmetry (point group C_{2h}) [38]. An energy dispersive X-ray spectroscopy (EDX) spectrum for a 10-layer GaTe film (8 nm) was obtained, and the atomic ratio of Ga/Te was identified to be 1, which is consistent with the determined structure, with a standard deviation of less than 5% across the entire wafer. For the HRTEM experiments, GaTe was peeled off from the mica substrate and transferred onto a copper grid (Fig. 1(d) inset). A typical HRTEM image is presented in Fig. 1(d) and reveals the perfect crystalline quality.

Raman spectroscopy was employed to understand the phonon vibration modes. Figure 1(e) presents the normalized Raman spectra acquired from GaTe thin films with different thickness, in which three dominant peaks can be observed that correspond to the A_g modes in GaTe, identical to the exfoliated ultrathin GaTe sheets [35]. The fact that the peak at 114 cm^{-1} arises upon increasing the thickness of GaTe suggests the phonon modes occurring in our GaTe thin films, which are similar to those in the exfoliated GaTe sheets [35]. It is also noted that the distance between the left two peaks strongly depends on the thickness, similar to few-layer MoS_2 [39]. The peak distance increases from 10.0 to 14.5 cm^{-1} when the number of layers decreases from 28 to 2 (Fig. 1(e)). For this reason, Raman spectroscopy can serve as a sensitive probe to identify the layers of GaTe and verify the film quality as well as providing evidence of the good control of thickness achievable using the MBE technique.

Temperature-dependent Hall measurements were also performed to evaluate the electrical properties of the 8-nm-thick GaTe thin film grown on the mica substrate. The Hall bar devices were fabricated in the centimeter range. Indium was soldered as electrodes and formed a perfect Ohmic contract (Fig. S1 in the Electronic Supplementary Material (ESM)). Surprisingly, the result reveals p-type conductivity with a room-temperature hole mobility reaching 28.4 $cm^2/(V·s)$ (Fig. S2 in the ESM), the highest mobility reported for ultrathin GaTe sheets thus far. The absorption spectrum measurements (Fig. S12 in the ESM) exhibit a 1.65-eV thickness-independent direct bandgap of few-layer GaTe, consistent with our XRD results and previously report theoretical calculations [35]. The unexpected high mobility and direct bandgap make the GaTe a promising candidate for realizing highly efficient devices.

For their practical applications, the GaTe thin films were directly deposited on three-inch n-doped Si (100) substrates under the optimized growth conditions to construct vertical p-n junctions. To investigate the atomic composition, the EDX spectrum was collected from the cross-section TEM specimen of a 50-layer-thick GaTe sample (Fig. 2(a)). The atomic ratio of Ga and Te was deduced to be approximately 1. Note that the detected Cu signals originate from the copper grid. The inset shows an EDX mapping of the Ga and Te

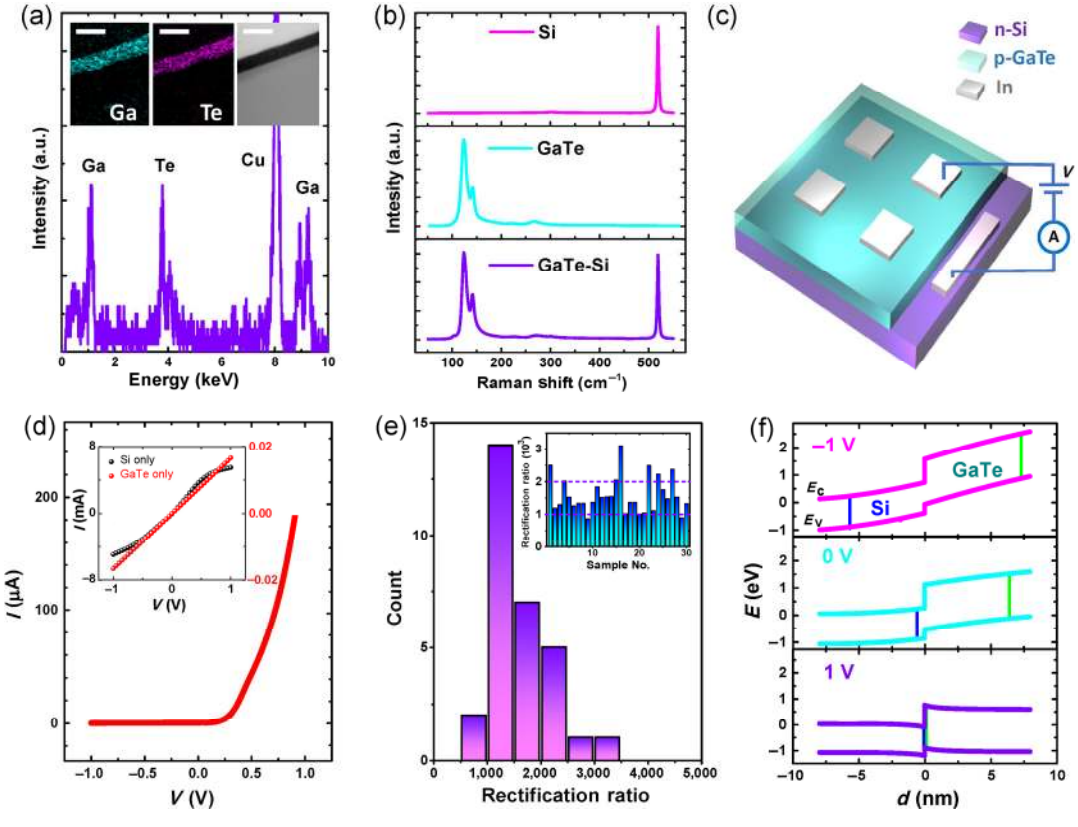

Figure 2 Electrical characterization and EDX and Raman spectra of the 10-layer GaTe/Si p-n junctions. (a) A typical EDX spectrum acquired from the few-layer GaTe grown on Si. The atomic ratio of Ga/Te reaches 1 within the accuracy of the equipment. The inset presents a TEM image and the elemental distribution mappings of Ga and Te obtained from the HRTEM/EDX analysis, revealing the uniform element distribution. The scale bar represents 100 nm. (b) Raman spectra acquired from the area of Si, GaTe/mica, and the junction area. Both GaTe and Si peaks are detected in the junction area. (c) A schematic view of the device structure. (d) The rectifying *I*–*V* characteristics of the device. The inset shows the Ohmic contact for In–GaTe, whereas In–Si exhibits a negligible barrier. (e) A histogram of the rectification ratio distribution based on 30 randomly selected diodes across a three-inch GaTe/Si wafer. The inset shows the rectification ratio for an individual diode. (f) Calculated band diagrams of GaTe/Si junction under various bias conditions. The space–charge regime (between the two vertical lines) can be significantly decreased with positive bias, which explains the high rectification ratio. GaTe is almost depleted at zero and negative bias.

elements, demonstrating their uniform distribution in the thin films. Hereafter, we will concentrate on the 10-layer-thick GaTe for evaluating the device performance unless otherwise mentioned. In addition, the results for the 4-layer-thick GaTe are provided in the ESM. Figure 2(b) presents the Raman spectra of Si, GaTe/mica, and GaTe/Si in the upper, middle, and bottom panel, respectively. In the GaTe/Si heterojunction, both peaks from Si and GaTe can be well resolved. Importantly, reminiscent of the GaTe grown on mica (Fig. 1(e)), the left two prominent peaks are located at the same wavenumbers, indicating the comparable crystalline quality and film thickness.

To understand its electrical properties, we further conducted electrical measurements to examine the device performance, as schematically illustrated in Fig. 2(c). Indium was employed as the metal electrodes for both Si and GaTe using simple soldering. A clear rectifying characteristic is observed in the current–voltage (*I*–*V*) measurements (Fig. 2(d)). The rectification ratio, defined as the ratio of the forward and reverse current, reaches ~10^3 under *I*–*V* bias at 300 K. The inset of Fig. 2(d) shows the perfect Ohmic contact on GaTe (the red curve), whereas on Si, a negligible barrier exists that does not significantly affect the rectifying characteristic. These devices can also work at low temperatures with 20-times higher rectification ratios as the temperature decreases to 150 K, as observed in Fig. S5 (in the ESM). To study the device statistics, 30 diodes across the wafer were randomly selected, and their *I*–*V* characteristics were recorded.

Numerical simulation was performed to elucidate the device operating principles. Figure 2(f) presents the energy-band diagrams of the p-n junction under a voltage bias (V = ±1 V) and equilibrium condition (0 V). At equilibrium, a one-sided abrupt junction or n^+p heterojunction is formed as the carrier concentration in the heterojunction changes abruptly from electrons of $N_e = 6.38 \times 10^{18}$ cm^{-3} to holes of $N_h = 2.5 \times 10^{18}$ cm^{-3}, as observed in the middle panel. Note that nearly 90% of the GaTe epitaxial layer is depleted under the thermal equilibrium condition, which makes the 2D GaTe a good photo-absorption and carrier-generating layer. The total thickness of the space charge regime expands almost two times under the reverse bias (–1 V) compared with that under the zero bias. The depletion layer entirely disappears under the forward bias of +1 V, which is consistent with the *I*–*V* characteristics (Fig. 2(d)).

To allow the highest possible absorption of light in the photodiodes, a transparent 50-nm-thick indium-tin oxide (ITO) layer was deposited on top of GaTe as the anode electrodes (Fig. 3(a)). ITO has a good transmittance in the visible range [40] through which the light can mostly reach the vertical junction. The formation of the Ohmic contact was also confirmed as the prerequisite for high-efficiency devices [41] (Fig. S6 in the ESM). The lower panel presents a photograph of the real sample on which a periodic arrangement of photodiodes can be observed (purple squares). Figure 3(b) presents the negatively biased *I*–*V* characteristics under laser illumination (632 nm focused laser). The reverse current increases dramatically upon increasing the incident power, suggesting the generation of the photocurrent, which is defined by the difference between the illuminated and non-illuminated current ($I_{ph} = I_{light} - I_{dark}$).

The extracted photocurrent increases with the incident power following a power law (Fig. 3(c)), which results from the increased photocarriers under strong illumination. However, the photocarrier generation saturates at a high incident power, causing the drop of EQE, as observed in Fig. 3(d). Here, the EQE is defined as the ratio of collected charge carrier to incident photon, i.e., $\mathrm{EQE} = \frac{I_{ph}}{q\phi} = \frac{I_{ph}}{q}\frac{h\upsilon}{P_{in}}$, where I_{ph} is the photocurrent, ϕ is the incident photon flux, $h\upsilon$ is the energy of a single photon, q is the electron charge, and P_{in} is the incident power of light. The measured EQE for our diodes reaches an unexpectedly high value of 62% at 4.8 μW and zero bias. The dark current at zero bias is smaller than 50 pA (the photocurrent is on the order of μA) indicating no influential residue bias in the system. Normally, the EQE is less than 1. Such a high EQE is attributed to the high absorption rate of the device (Fig. S11 in the ESM) and the direct bandgap of GaTe (Fig. S12 in the ESM), which cause highly efficient carrier excitations [8, 42, 43]. Other parameters are also extracted for the 4.8-μW data near zero bias. The responsivity defined as the ratio between the photocurrent and input power is 0.32 A/W. In addition, we observe a lower

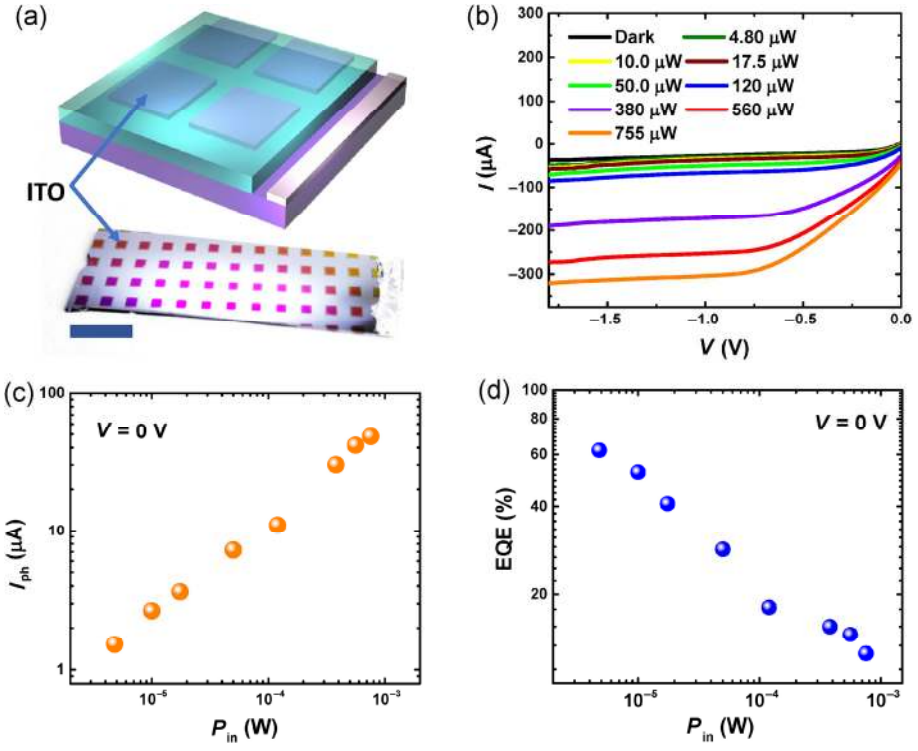

Figure 3 Photoresponse of 10-layer GaTe/Si p-n junctions. (a) A schematic view of the device structure, which shares the same legends with Fig. 2(c). The lower panel presents a photograph of a real sample on which a periodic arrangement of devices can be observed (colored area). The bar represents 5 mm. (b) Negatively biased *I*–*V* characteristics under the 632.8-nm laser illumination. When the laser intensity increases, the current systemically rises up to 322 μA, suggesting a high photosensitivity. (c) Photocurrent under different incident power. (d) EQE versus incident power at zero bias. A relatively high EQE value of 62% can be achieved at 4.8 μW.

EQE (40%) from thinner samples. More detailed data and discussions are available in Fig. S9 (in the ESM).

In addition to the superior photoresponsivity and good external quantum efficiency, we conducted time-resolved photoresponse experiments by periodically turning on and off the laser illumination at a frequency of 761 Hz and recording the signal from an oscilloscope. Figure 4(a) presents a complete on/off circle during the operation in which the photocurrent exhibits a rapid rise and reaches a steady saturation. To quantitatively analyze the response speed in a time frame, we performed a best fit of the rising and falling components, as presented in Fig. 4(b). The rising edge is perfectly fitted, overlapping with the single exponential function following $I_{ph} = I_{sat}(1-e^{-(t-t_0)/\tau})$ and yielding a time constant of 22 μs, which is relatively fast for state-of-the-art 2D semiconductors. Although the falling part cannot be completely fitted, the sharp edge indicates that the response time should be much less than 22 μs (the inset of Fig. 4(b)). Furthermore, the signals recorded by the oscilloscope remain nearly unchanged after 1.37 million cycles of operation (Fig. 4(c)), pointing to the excellent stability and reliability of the photodiodes.

To further probe the photoresponse characteristics of the devices, we performed spatially resolved photocurrent measurements by incorporating a galvanometer into the light path (Fig. 4(d)). The generated photocurrent is uniformly distributed in the junction area (a corner of the device), and the spatial mapping precisely matches the device geometry, as shown in the inset of Fig. 4(a). The statistics of the device concerning the photoresponse performance were also analyzed similar to what was performed for the electrical test (Fig. 2(e)). The incident power was increased to 380 μW to make the laser spot easily visible. The photocurrent is mainly distributed in the range of 20 to 40 μA, occupying 73% of 30 randomly selected photodiodes (Fig. 4(e)). Only 6% of samples exhibit a photocurrent below 20 μA, revealing good

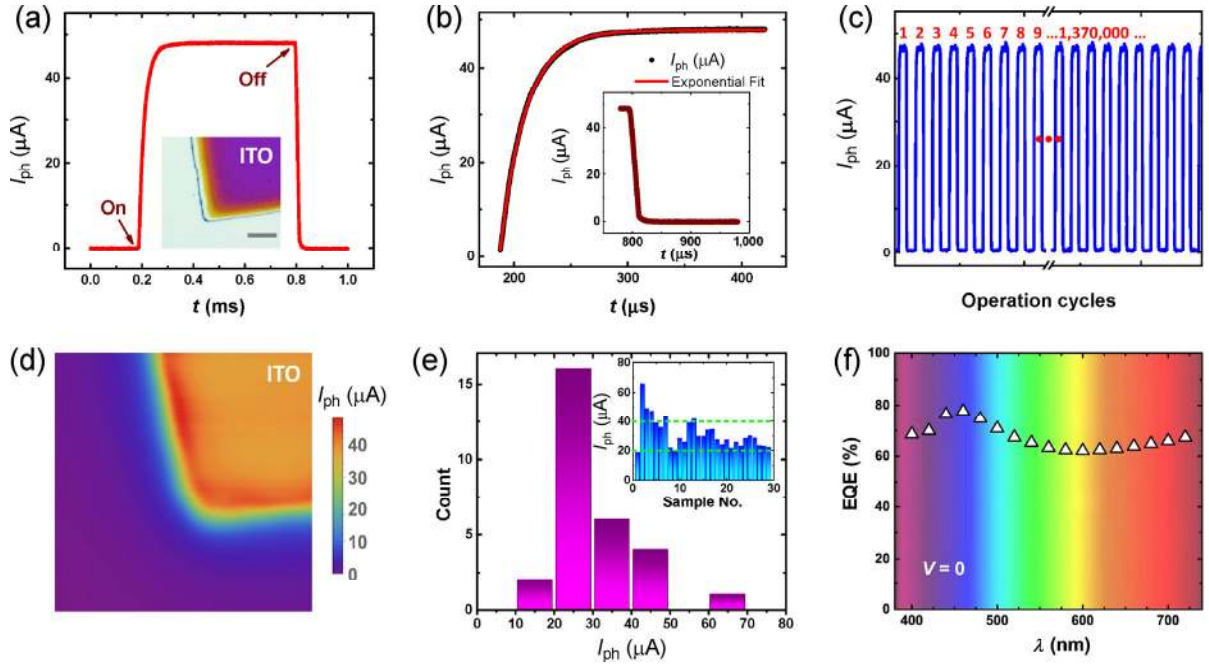

Figure 4 Time-, spatial-, and wavelength-resolved photoresponse measurements and device repeatability. (a) Time-resolved photoresponse with incident laser power of 4.8 μW. The inset presents a microscopic picture from a corner of the device. The bar represents 0.1 mm. (b) Time-resolved photoresponse. When illuminated, the photocurrent rises rapidly to reach saturation within a time constant of 22 μs. The black and red curves are the experimental data and exponential fit, respectively. The inset is the falling part of the photocurrent, showing a faster decay with a time constant less than 22 μs. (c) Photocurrent response during 1.37 million cycles of operation. The device exhibits an endurable photoresponse. (d) A spatial mapping of the photocurrent from a corner of the diode. The generated photocurrent is uniformly distributed in the junction area. The spatial mapping precisely matches the device geometry, as observed in the inset in (a). (e) A histogram of the photocurrent distribution based on 30 randomly selected photodiodes. The inset shows the photocurrent for an individual diode. They were measured at zero bias under an incident power of 380 μW. (f) Wavelength-dependent EQE at zero bias under an incident power of 5 μW. The color of the background is consistent with the wavelength. The GaTe/Si junctions exhibit a uniform and high EQE in the visible range.

repeatability. Wavelength-dependent photoresponse measurements were also performed in the visible range under an incident power of 5 μW. Inspiringly, the photoresponse of the diodes covers nearly the entire range of 400–750 nm (Fig. 4(f)). The absorption spectrum (Fig. S13 in the ESM) of pure GaTe reveals a distinct photovoltaic contribution from the 2D GaTe layers, particularly for wavelengths less than 650 nm. However, for wavelengths higher than 650 nm, GaTe cannot absorb the light efficiently. However, single-crystal Si exhibits very high EQE in this region. Thus, the GaTe and Si compensate for each other, covering the photoresponse of the entire visible range. Moreover, the steady EQE (>60%) in the entire visible spectrum makes the GaTe/Si diodes applicable for broadband detection or solar cells with high efficiency.

Although the arrayed GaTe/Si p-n junctions exhibited a super-fast, broadband and repeatable photoresponse, they are still at the early age of proof-of-concept. Significant progress must be made toward the practical utilization of 2D materials. With this in mind, we replaced the CCD unit in a digital camera with our GaTe/Si photodiodes connected to a pre-amplifier. Then, the camera with GaTe/Si sensors was placed on a piezoelectric platform, as illustrated in Fig. 5 (left upper panel). By scanning the stage in different directions, the spatial photoresponse could be recorded as a function of 2D coordinates. Using this technique, several images of printed objects were taken with reasonable contrast and spatial resolution: "Fudan & SITP", "two-dimensional material" (in Chinese), and an official logo of Fudan University. With the combination of 2D materials and traditional silicon technology, it is possible to realize commercial devices upon further improvement of the fabrication process and material synthesis.

Figure 5 Experimental set-up and image acquisition by GaTe/Si photodiodes. The left upper panel shows the experimental set-up, including the piezoelectric platform, camera, and target. All the other panels are the images taken by the GaTe/Si diodes with reasonable contrast and spatial resolution: "Fudan & SITP", "two-dimensional material" (in Chinese), and an official logo of Fudan University. The scale bar is 50 mm.

3 Conclusions

In conclusion, we achieved controllable layer-by-layer growth of GaTe using MBE. Few-layer GaTe forms wafer-scale arrayed *p-n* junctions on Si with high yield and repeatable electrical and optical characteristics. Importantly, they can be used as photodiodes with sensitive, fast, stable, and broadband photoresponse. The capability of acquiring real images using the GaTe/Si heterojunctions demonstrates the potential for the 2D materials for practical applications.

4 Method

4.1 Thin-film synthesis

Few-layer GaTe was grown on fleshly cleaved mica or silicon substrates in a Perkin Elmer 430 MBE system. Standard Knudsen cells provided high-purity Ga and Te fluxes. Typically, the film growth was conducted under Te-rich conditions with a Ga/Te ratio of 1:20 measured by a crystal oscillator. The growth temperature was maintained at 600 ℃.

4.2 Characterization tools

The surface morphology was examined using an AFM (Park System E-120) in tapping mode. Raman spectroscopy measurements were performed with an incident laser wavelength of 632.8 nm (Renishaw inVia confocal Raman system). The laser spot was focused with a diameter of 3 μm. The structural properties were investigated using an HRTEM (FEI Tecnai F20) and XRD (Bruker D8 Discover). Temperature-dependent Hall measurements were conducted using a Quantum Design physical property measurement system (PPMS) with a maximum magnetic field of 9 T.

4.3 Electrical and optoelectrical characterization

Electrical characteristics and photoresponse measurements were performed using an Agilent 2902. The voltage accuracy was 0.1 μV. The incident light from a 632.8-nm laser was focused on the samples. The intensity was controlled using a series of neutral density filters and a linear polarizer/wave-plate and calibrated using a Thorlab-S130C photodiode photo sensor. For the time-resolved photocurrent measurements, the laser illumination was controlled by a Thorlab-ITC4001 controller, working at a chopping frequency of 761 Hz. A Tektronix MDO 3014 oscilloscope was used to read the signals. For the spatially resolved photocurrent measurements, a galvanometer was controlled by an open-source controller, thus allowing laser spot scanning across the device. For the wavelength-resolved measurements, a Horiba spectrometer combined with a halogen lamp was used, covering the visible range.

4.4 Imaging

A digital camera was dissembled. The CCD unit was replaced by the GaTe/Si diodes. The signal was amplified by a pre-amplifier (Stanford Research System 560) and collected using a home-built acquisition system. By simultaneously monitoring the controller position and photoelectric signal, the imaging was achieved.

4.5 Numerical simulations

To investigate the energy-band diagrams in the n^+p heterojunction under different bias conditions, 2D steady-state numerical simulations were performed using the Sentaurus Device, a commercial software package from Synopsys. For the plain drift-diffusion simulation, the well-known Poisson equation and continuity equations were used in the calculations. The carrier generation–recombination process consisted

of Shockley–Read–Hall, Auger, and radiative terms. Additionally, tunneling effects, such as band-to-band and trap-assisted tunneling, were included in the simulation.

Acknowledgements

This work was supported by the National Young 1000 Talent Plan, Pujiang Talent Plan in Shanghai, National Natural Science Foundation of China (Nos. 61322407, 11474058, and 11322441), the Chinese National Science Fund for Talent Training in Basic Science (No. J1103204), and Ten Thousand Talents Program for young talents. Part of the sample fabrication was performed at Fudan Nano-fabrication Laboratory. We acknowledge Yuanbo Zhang, Yizheng Wu, Zuimin Jiang, Likai Li, Boliang Chen for great assistance during the device fabrication and measurements.

Electronic Supplementary Material: Supplementary material (contact measurement, sample photos, temperature-dependent measurement and photoresponse for 4-layer sample) is available in the online version of this article at http://dx.doi.org/10.1007/s12274-015-0833-8.

References

[1] Dean, C. R.; Young, A. F.; Meric, I.; Lee, C.; Wang, L; Sorgenfrei, S.; Watanabe, K.; Taniguchi, T.; Kim, P.; Shepard, K. L. et al. Boron nitride substrates for high-quality graphene electronics. *Nat. Nanotechnol.* **2010**, *5*, 722–726.

[2] Liu, M.; Yin, X. B.; Ulin-Avila, E.; Geng, B. S.; Zentgraf, T.; Ju, L.; Wang, F.; Zhang, X. A graphene-based broadband optical modulator. *Nature* **2011**, *474*, 64–67.

[3] Wang, X. M.; Cheng, Z. Z.; Xu, K.; Tsang, H. K.; Xu, J. B. High-responsivity graphene/silicon-heterostructure waveguide photodetectors. *Nat. Photonics* **2013**, *7*, 888–891.

[4] Pospischil, A.; Humer, M.; Furchi, M. M.; Bachmann, D.; Guider, R.; Fromherz, T.; Mueller, T. CMOS-compatible graphene photodetector covering all optical communication bands. *Nat. Photonics* **2013**, *7*, 892–896.

[5] Xia, F. N.; Mueller, T.; Lin, Y. M.; Valdes-Garcia, A.; Avouris, P. Ultrafast graphene photodetector. *Nat. Nanotechnol.* **2009**, *4*, 839–843.

[6] Sun, D.; Aivazian, G.; Jones, A. M.; Ross, J. S.; Yao, W.; Cobden, D.; Xu, X. D. Ultrafast hot-carrier-dominated photocurrent in graphene. *Nat. Nanotechnol.* **2012**, *7*, 114–118.

[7] Liu, C. H.; Chang, Y. C.; Norris, T. B.; Zhong, Z. H. Graphene photodetectors with ultra-broadband and high responsivity at room temperature. *Nat. Nanotechnol.* **2014**, *9*, 273–278.

[8] Sun, Z. H.; Chang, H. X. Graphene and graphene-like two-dimensional materials in photodetection: Mechanisms and methodology. *ACS Nano* **2014**, *8*, 4133–4156.

[9] Huang, X.; Yin, Z. Y.; Wu, S. X.; Qi, X. Y.; He, Q. Y.; Zhang, Q. C.; Yan, Q. Y.; Boey, F.; Zhang, H. Graphene-based materials: Synthesis, characterization, properties, and applications. *Small* **2011**, *7*, 1876–1902.

[10] Radisavljevic, B.; Radenovic, A.; Brivio, J.; Giacometti, V.; Kis, A. Single-layer MoS_2 transistors. *Nat. Nanotechnol.* **2011**, *6*, 147–150.

[11] Li, H.; Wu, J.; Yin, Z. Y.; Zhang, H. Preparation and applications of mechanically exfoliated single-layer and multilayer MoS_2 and WSe_2 nanosheets. *Acc. Chem. Res.* **2014**, *47*, 1067–1075.

[12] Yin, Z. Y.; Li, H.; Li, H.; Jiang, L.; Shi, Y. M.; Sun, Y. H.; Lu, G.; Zhang, Q.; Chen, X. D.; Zhang, H. Single-layer MoS_2 phototransistors. *ACS Nano* **2011**, *6*, 74–80.

[13] Deng, Y. X.; Luo, Z.; Conrad, N. J.; Liu, H.; Gong, Y. J.; Najmaei, S.; Ajayan, P. M.; Lou, J.; Xu, X. F.; Ye, P. D. Black phosphorus–monolayer MoS_2 van der Waals heterojunction p–n diode. *ACS Nano* **2014**, *8*, 8292–8299.

[14] Yan, K.; Wu, D.; Peng, H. L.; Jin, L.; Fu, Q.; Bao, X. H.; Liu, Z. F. Modulation-doped growth of mosaic graphene with single-crystalline p–n junctions for efficient photocurrent generation. *Nat. Commun.* **2012**, *3*, 1280.

[15] Mak, K. F.; Lee, C.; Hone, J.; Shan, J.; Heinz, T. F. Atomically thin MoS_2: A new direct-gap semiconductor. *Phys. Rev. Lett.* **2010**, *105*, 136805.

[16] Yu, W. J.; Li, Z.; Zhou, H. L.; Chen, Y.; Wang, Y.; Huang, Y.; Duan, X. F. Vertically stacked multi-heterostructures of layered materials for logic transistors and complementary inverters. *Nat. Mater.* **2013**, *12*, 246–252.

[17] Hu, P. A.; Zhang, J.; Yoon, M.; Qiao, X. F.; Zhang, X.; Feng, W.; Tan, P. H.; Zheng, W.; Liu, J. J.; Wang, X. N. et al. Highly sensitive phototransistors based on two-dimensional GaTe nanosheets with direct bandgap. *Nano Res.* **2014**, *7*, 694–703.

[18] Ross, J. S.; Klement, P.; Jones, A. M.; Ghimire, N. J.; Yan, J. Q.; Mandrus, D. G.; Taniguchi, T.; Watanabe, K.; Kitamura, K.; Yao, W. et al. Electrically tunable excitonic light-emitting diodes based on monolayer WSe_2 p–n junctions. *Nat. Nanotechnol.* **2014**, *9*, 268–272.

[19] Fang, H.; Battaglia, C.; Carraro, C.; Nemsak, S.; Ozdol, B.; Kang, J. S.; Bechtel, H. A.; Desai, S. B.; Kronast, F.; Unal, A. A. Strong interlayer coupling in van der Waals

heterostructures built from single-layer chalcogenides. *Proc. Natl. Acad. Sci. USA* **2014**, *111*, 6198–6202.

[20] Geim, A. K.; Grigorieva, I. V. van der Waals heterostructures. *Nature* **2013**, *499*, 419–425.

[21] Yu, L. L.; Lee, Y. H.; Ling, X.; Santos, E. J. G.; Shin, Y. C.; Lin, Y. X.; Dubey, M.; Kaxiras, E.; Kong, J.; Wang, H. et al. Graphene/MoS_2 hybrid technology for large-scale two-dimensional electronics. *Nano Lett.* **2014**, *14*, 3055–3063.

[22] Gong, Y. J.; Lin, J. H.; Wang, X. L.; Shi, G.; Lei, S. D.; Lin, Z.; Zou, X. L.; Ye, G. L.; Vajtai, R.; Yakobson, B. I. et al. Vertical and in-plane heterostructures from WS_2/MoS_2 monolayers. *Nat. Mater.* **2014**, *13*, 1135–1142.

[23] Georgiou, T.; Jalil, R.; Belle, B. D.; Britnell, L.; Gorbachev, R. V.; Morozov, S. V.; Kim, Y. J.; Gholinia, A.; Haigh, S. J.; Makarovsky, O. et al. Vertical field-effect transistor based on graphene-WS_2 heterostructures for flexible and transparent electronics. *Nat. Nanotechnol.* **2013**, *8*, 100–103.

[24] Huang, C. M.; Wu, S. F.; Sanchez, A. M.; Peters, J. J. P.; Beanland, R.; Ross, J. S.; Rivera, P.; Yao, W.; Cobden, D. H.; Xu, X. D. Lateral heterojunctions within monolayer $MoSe_2$-WSe_2 semiconductors. *Nat. Mater.* **2014**, *13*, 1096–1101.

[25] Gu, X.; Cui, W.; Li, H.; Wu, Z. W.; Zeng, Z. Y.; Lee, S. T.; Zhang, H.; Sun, B. Q. A solution-processed hole extraction layer made from ultrathin MoS_2 nanosheets for efficient organic solar cells. *Adv. Energy Mater.* **2013**, *3*, 1262–1268.

[26] Chen, J. Z.; Wu, X. J.; Yin, L. S.; Li, B.; Hong, X.; Fan, Z. X.; Chen, B.; Xue, C.; Zhang, H. One-pot synthesis of CdS nanocrystals hybridized with single-layer transition-metal dichalcogenide nanosheets for efficient photocatalytic hydrogen evolution. *Angew. Chem.* **2014**, *127*, 1226–1230.

[27] Pospischil, A.; Furchi, M. M.; Mueller, T. Solar-energy conversion and light emission in an atomic monolayer p–n diode. *Nat. Nanotechnol.* **2014**, *9*, 257–261.

[28] Zhang, W. J.; Chuu, C.-P.; Huang, J.-K.; Chen, C.-H.; Tsai, M.-L.; Chang, Y.-H.; Liang, C.-T.; Chen, Y.-Z.; Chueh, Y.-L.; He, J.-H. et al. Ultrahigh-gain photodetectors based on atomically thin graphene-MoS_2 heterostructures. *Sci. Rep.* **2014**, *4*, 3826.

[29] Yin, Z. Y.; Zhang, X.; Cai, Y. Q.; Chen, J. Z.; Wong, J. I.; Tay, Y. Y.; Chai, J. W.; Wu, J.; Zeng, Z. Y.; Zheng, B. et al. Preparation of MoS_2–MoO_3 hybrid nanomaterials for light–emitting diodes. *Angew. Chem.* **2014**, *126*, 12768–12773.

[30] Zhang, J.; Zhu, Z. P.; Feng, X. L. Construction of two-dimensional MoS_2/CdS p–n nanohybrids for highly efficient photocatalytic hydrogen evolution. *Chem.—Eur. J.* **2014**, *20*, 10632–10635.

[31] Lopez-Sanchez, O.; Lembke, D.; Kayci, M.; Radenovic, A.; Kis, A. Ultrasensitive photodetectors based on monolayer MoS_2. *Nat. Nanotechnol.* **2013**, *8*, 497–501.

[32] Choi, M. S.; Qu, D. S.; Lee, D.; Liu, X. C.; Watanabe, K.; Taniguchi, T.; Yoo, W. J. Lateral MoS_2 p–n junction formed by chemical doping for use in high-performance optoelectronics. *ACS Nano* **2014**, *8*, 9332–9340.

[33] Yu, W. J.; Liu, Y.; Zhou, H. L.; Yin, A. X.; Li, Z.; Huang, Y.; Duan, X. F. Highly efficient gate-tunable photocurrent generation in vertical heterostructures of layered materials. *Nat. Nanotechnol.* **2013**, *8*, 952–958.

[34] Lee, C. H.; Lee, G. H.; van der Zande, A. M.; Chen, W. C.; Li, Y. L.; Han, M. Y.; Cui, X.; Arefe, G.; Nuckolls, C.; Heinz, T. F. et al. Atomically thin p–n junctions with van der Waals heterointerfaces. *Nat. Nanotechnol.* **2014**, *9*, 676–681.

[35] Liu, F. C.; Shimotani, H.; Shang, H.; Kanagasekaran, T.; Zólyomi, V.; Drummond, N.; Fal'ko, V. I.; Tanigaki, K. High-sensitivity photodetectors based on multilayer GaTe flakes. *ACS Nano* **2014**, *8*, 752–760.

[36] Peng, H. L.; Dang, W. H.; Cao, J.; Chen, Y. L.; Wu, D.; Zheng, W. S.; Li, H.; Shen, Z.-X.; Liu, Z. F. Topological insulator nanostructures for near-infrared transparent flexible electrodes. *Nat. Chem.* **2012**, *4*, 281–286.

[37] Wang, Z. X.; Xu, K.; Li, Y. C.; Zhan, X. Y.; Safdar, M.; Wang, Q. S.; Wang, F. M.; He, J. Role of Ga vacancy on a multilayer GaTe phototransistor. *ACS Nano* **2014**, *8*, 4859–4865.

[38] Wan, J. Z.; Brebner, J. L.; Leonelli, R.; Graham, J. T. Optical properties of excitons in GaTe. *Phys. Rev. B* **1992**, *46*, 1468–1471.

[39] Lee, C.; Yan, H. G.; Brus, L. E.; Heinz, T. F.; Hone, J.; Ryu, S. Anomalous lattice vibrations of single- and few-layer MoS_2. *ACS Nano* **2010**, *4*, 2695–2700.

[40] Granqvist, C. G.; Hultåker, A. Transparent and conducting ITO films: New developments and applications. *Thin Solid Films* **2002**, *411*, 1–5.

[41] Ng, W. L.; Lourenço, M. A.; Gwilliam, R. M.; Ledain, S.; Shao, G.; Homewood, K. P. An efficient room-temperature silicon-based light-emitting diode. *Nature* **2001**, *410*, 192–194.

[42] Zólyomi, V.; Drummond, N. D.; Fal'ko, V. I. Band structure and optical transitions in atomic layers of hexagonal gallium chalcogenides. *Phys. Rev. B.* **2013**, *87*, 195403.

[43] Sánchez-Royo, J. F.; Pellicer-Porres, J.; Segura, A.; Muñoz-Sanjosé, V.; Tobías, G.; Ordejón, P.; Canadell, E.; Huttel, Y. Angle-resolved photoemission study and first-principles calculation of the electronic structure of GaTe. *Phys. Rev. B.* **2002**, *65*, 115201.